Information Sharing Between Localization, Tracking, and Identification Algorithms

Richard J. Kozick
Bucknell University
Department of Electrical Engineering
Lewisburg, PA 17837

Brian M. Sadler
Army Research Laboratory
AMSRL-CI-CN
2800 Powder Mill Road
Adelphi, MD 20783

September 24, 2002

Abstract

Algorithms for ground vehicle classification using acoustic measurements often use features based on the relative amplitudes of harmonic components. The average power measured at each harmonic frequency fluctuates due to scattering of the acoustic waves during propagation and additive noise at the sensor. In this paper, we use propagation models for frequency-dependent scattering of acoustic signals to study the performance and limitations of ground vehicle classifiers that use harmonic amplitudes as the features. The harmonic amplitudes for a given vehicle may vary due to other factors besides scattering, such as engine load and speed (revving) and the orientation of the source with respect to the sensor (aspect angle). Information about vehicle speed and aspect angle are available from localization and tracking algorithms in a networked sensor system. We evaluate the potential for improved classification accuracy when additional features are used from the localization and tracking algorithm. Examples from measured data are included to illustrate the results.

1   Introduction

Networks of aeroacoustic and seismic sensors are used to collect data for the purposes of localizing the positions of ground vehicles, tracking the vehicles as they move, and identifying the vehicle types [1]. The localization, tracking, and identification algorithms often operate in parallel and with minimal sharing of information. The performance of all three algorithms can be improved with additional information sharing and signal processing. Examples of information sharing include predicted source locations (from the tracking algorithm to aid the localization algorithm), differential Doppler (from the sensor nodes to aid data association in the tracking algorithm), and source aspect angle/range/velocity (from the tracking algorithm to aid identification based on features from nodes).

Our focus in this paper is on the problem of identifying (or classifying) the type of vehicle from its acoustic signature. The objective is to broadly classify the vehicle into tracked and wheeled categories, and to further identify the vehicle type within these categories. Most classification algorithms that have been developed for this problem use the relative amplitudes of harmonic components in the acoustic signal as features to distinguish between vehicle types [2]–[9]. However,

the harmonic amplitudes for a given source may vary significantly due to several factors. For example, the target range, land topography, and meteorological conditions determine the extent of signal fluctuations caused by frequency-dependent scattering of the acoustic waves as they propagate through the air. The harmonic amplitudes also vary due to engine speed (revving) and the orientation of the source with respect to the sensor (aspect angle).

We study the limitations on classification accuracy caused by scattering during propagation using models developed in [10, 11, 12, 13]. The models are developed in detail in Section 2, but an overview is as follows. Consider the acoustic signal measured at one sensor when a vehicle is in close range. The measured signal is modeled as a sum of L harmonics with fundamental frequency f_0 Hz observed in additive, white, Gaussian noise. The harmonic amplitudes measured at the sensor include the effects of propagation (deterministic power loss and random scattering), source aspect angle, and Doppler. We consider a simple and commonly used processing strategy in which the received average signal power is estimated in L narrow frequency bands centered at the harmonics $f_0, 2f_0, \ldots, Lf_0$. Let us define the following for each band, $l = 1, \ldots, L$:

P_l =average power of the measured signal at the sensor,
   including the effects of scattering and noise

S_l =average signal power when there is no noise

$2\sigma_n^2$ =average noise power (same for each band)

Ω_l ="saturation" parameter characterizing the amount of scattering, with $0 \leq \Omega_l \leq 1$ and
   $0 =$ no scattering (an entirely deterministic signal), and
   $1 =$ complete scattering (an entirely random signal).

The "signature" of harmonic powers, $S_1, S_2, \ldots, S_L$, is commonly used for source classification. The measurable quantities are the *received* signal powers $P_1, P_2, \ldots, P_L$, so the classification performance depends on the variation of P_l with respect to the unscattered S_l.

In this paper, we investigate methods for improved classification accuracy by performing additional averaging to reduce the harmonic signature fluctuations due to scattering. We also investigate the feasibility of simple methods to incorporate range, speed, and aspect angle information from the tracking algorithm to improve the classification performance. Our recommendation based on the propagation model and measured data is to characterize each source of interest with three signatures: one at the closest point of approach (CPA), the second at aspect angles in which the *front* of the vehicle is observed, and the third at aspect angles in which the *rear* of the vehicle is observed. The multiple aspects of the vehicle may be obtained from a single sensor over time as the vehicle moves, or from multiple sensors that observe the vehicle at the same time. Moving vehicles are observed many times at the front and rear aspects, so the harmonic signatures may be averaged at these aspects to reduce the fluctuations due to scattering. Classification is then performed using the signature at CPA and the average signatures at the front and rear aspects.

The paper is organized as follows. The statistical model for the sensor data is presented in Section 2. This model is applied to classification performance in Section 3. The harmonic signature variations with range, speed, and aspect angle are evaluated in Section 4 using measured data, and Section 5 contains concluding remarks.

2 Model for Sensor Data with Scattering

In this section, we include a detailed review of the models developed in [10, 11, 12, 13], leading to the result that P_l is described by a noncentral chi-squared distribution. Then in Section 2.2 we review a model from [13] that relates the saturation Ω_l to the target range (r) and the frequency (lf_0). Classification performance based on these propagation models is considered in Section 3.

2.1 Scattering model

We begin by modeling the received signal at the fundamental frequency f_0 of the source. The extension to the higher harmonics will follow similarly. The measured signal $x(t)$ at the sensor is modeled as

$$x(t) = s(t) + n(t) \tag{1}$$

where $s(t)$ is the signal component caused by the acoustic source and $n(t)$ is a zero-mean, wide-sense stationary (WSS), additive white Gaussian noise (AWGN) process with power spectral density (PSD) $G_n(f) = \mathcal{N}_0/2$. The signal component is modeled as [10, 11, 12, 13]

$$s(t) = \sqrt{(1-\Omega)S} \, \cos(2\pi f_0 t + \theta) \, + \, v(t), \tag{2}$$

where $v(t)$ is a zero-mean, WSS, narrowband Gaussian random process with support in a frequency band of B Hz centered at f_0. That is, $v(t)$ has support in the frequency band $f_0 - B/2 \le |f| \le f_0 + B/2$, and the average power of $v(t)$ is

$$E\{v(t)^2\} = 2 \int_{f_0-B/2}^{f_0+B/2} G_v(f) \, df = \frac{\Omega S}{2}. \tag{3}$$

The signal component $s(t)$ in (2) is therefore a bandpass Gaussian random process with nonzero mean,

$$E\{s(t)\} = \sqrt{(1-\Omega)S} \, \cos(2\pi f_0 t + \theta) \tag{4}$$

$$\mathrm{Var}\{s(t)\} = E\{v(t)^2\} = \frac{\Omega S}{2}, \tag{5}$$

where the phase θ is a deterministic parameter. The average power (or mean-square value) of $s(t)$ is

$$\text{Average signal power} = \lim_{T \to \infty} \frac{1}{T} \int_{-T/2}^{T/2} s(t)^2 \, dt \tag{6}$$

$$= \lim_{T \to \infty} \frac{1}{T} \int_{-T/2}^{T/2} (1-\Omega)S \cos(2\pi f_0 t + \theta)^2 \, dt \, + \, E\{v(t)^2\} \tag{7}$$

$$= \frac{(1-\Omega)S}{2} + \frac{\Omega S}{2} = \frac{S}{2} \tag{8}$$

where in (7) we use the ergodicity of $v(t)$ to convert the time average to ensemble average. Thus the average power of the signal $s(t)$ is $S/2$, and the scattering model in (2) may be interpreted as follows. The saturation parameter $\Omega \in [0, 1]$ controls the allocation of power between the deterministic mean component, $(1-\Omega)S/2$, and the random (scattered) component, $\Omega S/2$. If $\Omega = 0$, then $s(t)$ is a deterministic sinusoid. If $\Omega = 1$, then $s(t) = v(t)$ is zero-mean, narrowband Gaussian noise. The case $0 < \Omega < 1$ is a combination, with some power in the sinusoidal component at f_0 Hz and the

remaining power scattered in a narrow band of width B Hz around f_0. For the measured signal model for $x(t)$ in (1), the scattered process $v(t)$ and the AWGN process $n(t)$ are assumed to be independent.

It is desirable to process $x(t)$ in the band of width B Hz around f_0 in order to collect all of the scattered signal energy. The scattered signal energy is useful for detecting the presence of sources as well as for direction finding, since the scattered components measured at distinct sensor locations are correlated with each other and may be used for time-difference-of-arrival processing. The deterministic mean component of $s(t)$ is also useful for source detection and direction finding. The structure shown in Figure 1 is commonly used to obtain the in-phase (I) and quadrature (Q) components of $x(t)$, which we denote by $x_i(t)$ and $x_q(t)$, respectively. Spectral estimates such as the spectrogram and FFT are often used to implement the processing in Figure 1, particularly when it is necessary to estimate the I and Q components at multiple frequencies. The lowpass filter in Figure 1 passes frequencies in the band $[-B/2, B/2]$ Hz, and the I and Q components have the form

$$x_i(t) = \sqrt{(1 - \Omega)S} \, \cos(\theta) \, + \, v_i(t) \, + \, n_i(t) \tag{9}$$

$$x_q(t) = \sqrt{(1 - \Omega)S} \, \sin(\theta) \, + \, v_q(t) \, + \, n_q(t), \tag{10}$$

where $v_i(t), n_i(t), v_q(t), n_q(t)$ are the I and Q components of the scattered signal $v(t)$ and the AWGN $n(t)$. The I and Q noise components have the properties

$$E\{v_i(t)^2\} = E\{v_q(t)^2\} = \int_{-B/2}^{B/2} G_{v_i}(f) \, df = \int_{-B/2}^{B/2} G_{v_q}(f) \, df$$

$$= \frac{\Omega S}{2} \, \triangleq \, \sigma_s^2 \tag{11}$$

$$G_{n_i}(f) = G_{n_q}(f) = \mathcal{N}_0 \tag{12}$$

$$E\{n_i(t)^2\} = E\{n_q(t)^2\} = \int_{-B/2}^{B/2} G_{n_i}(f) \, df = \int_{-B/2}^{B/2} G_{n_q}(f) \, df$$

$$= \mathcal{N}_0 \cdot B \, \triangleq \, \sigma_n^2, \tag{13}$$

where we have defined σ_s^2 and σ_n^2 in (11) and (13), respectively. The $x_i(t)$ and $x_q(t)$ processes in (9) and (10) are WSS, independent, and Gaussian with nonzero means. We can form the complex envelope

$$\widetilde{x}(t) = x_i(t) + jx_q(t) \tag{14}$$

$$= \widetilde{s}(t) \, + \, \widetilde{n}(t) \tag{15}$$

$$\widetilde{s}(t) = \sqrt{(1 - \Omega)S} \, e^{j\theta} \, + \, \widetilde{v}(t), \tag{16}$$

where $\widetilde{s}(t)$, $\widetilde{v}(t)$, and $\widetilde{n}(t)$ are complex envelope processes that are defined analogously to (14). The complex envelope $\widetilde{x}(t)$ is a WSS, complex, circular (the I and Q components are independent), Gaussian random process. We note the following relations:

$$E \, |\widetilde{s}(t)|^2 = |E\{\widetilde{s}(t)\}|^2 \, + \, \mathrm{Var}\{\widetilde{s}(t)\} \tag{17}$$

$$= (1 - \Omega)S \, + \, E \, |\widetilde{v}(t)|^2 \tag{18}$$

$$= (1 - \Omega)S \, + \, 2\sigma_s^2 = (1 - \Omega)S \, + \, \Omega S = S. \tag{19}$$
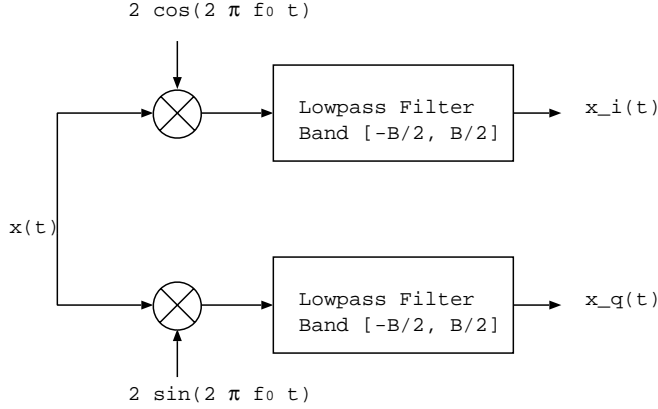
Figure 1: Processing to obtain in-phase and quadrature components, $x_i(t)$ and $x_q(t)$.

Therefore S is the average power (mean-square) of the signal component in the complex envelope representation. Note from (11) and (19) that the saturation is

$$\Omega = \frac{2\sigma_s^2}{S} = \frac{\text{Average scattered signal power}}{\text{Average received signal power}}, \tag{20}$$

and this is, in fact, the basic definition of saturation [10, 11, 12, 13]. The AWGN complex envelope has variance

$$\text{Var}\{\widetilde{n}(t)\} = E\,|\widetilde{n}(t)|^2 = 2\mathcal{N}_0 B \overset{\triangle}{=} 2\sigma_n^2. \tag{21}$$

We can characterize the probability distributions of $x_i(t)$ and $x_q(t)$ as independent, real-valued Gaussian pdfs,

$$x_i(t) \sim \text{N}\left(\sqrt{(1-\Omega)S}\cos\theta,\ \sigma_s^2 + \sigma_n^2\right) \tag{22}$$

$$x_q(t) \sim \text{N}\left(\sqrt{(1-\Omega)S}\sin\theta,\ \sigma_s^2 + \sigma_n^2\right). \tag{23}$$

Equivalently, the complex envelope has a circular, complex Gaussian pdf,

$$\widetilde{x}(t) \sim \text{CN}\left(\sqrt{(1-\Omega)S}\,e^{j\theta},\ 2\sigma_s^2 + 2\sigma_n^2\right) \tag{24}$$

$$\sim \text{CN}\left(\sqrt{(1-\Omega)S}\,e^{j\theta},\ \Omega S + 2\sigma_n^2\right), \tag{25}$$

which has the form

$$f(\widetilde{x}) = \frac{1}{2\pi(\Omega S + 2\sigma_n^2)/2}\,\exp\left(-\frac{1}{2}\frac{\left|\widetilde{x} - \sqrt{(1-\Omega)S}\,e^{j\theta}\right|^2}{(\Omega S + 2\sigma_n^2)/2}\right). \tag{26}$$

The complex envelope process $\widetilde{x}(t)$ is lowpass with bandwidth B Hz, so its samples are independent only when they are spaced by $> 1/B$ sec. Consider M samples $\widetilde{x}(t_1), \ldots, \widetilde{x}(t_M)$ with sample spacing $> 1/B$ sec so that the samples are modeled as statistically independent. The phase may vary from sample to sample, so the pdfs are

$$\widetilde{x}(t_m) \sim \text{CN}\left(\sqrt{(1-\Omega)S}\,e^{j\theta_m},\ \Omega S + 2\sigma_n^2\right), \quad m = 1, \ldots, M. \tag{27}$$

We consider coherent and incoherent combining of the M samples, as in [10, 11, 12, 13].

Coherent combining: For coherent combining, the phases $\theta_1, \ldots, \theta_M$ must be known (or assumed to be equal, since we are interested only in the average power P_C in (29)). The M samples are coherently combined to form

$$\widetilde{x}_C = \frac{1}{M} \sum_{m=1}^{M} \widetilde{x}(t_m)\, e^{-j\theta_m} \sim \text{CN}\left(\sqrt{(1-\Omega)S},\ \frac{\Omega S + 2\sigma_n^2}{M}\right), \tag{28}$$

and the average power of the measured signal for coherent combining is

$$P_C = |\widetilde{x}_C|^2 = x_{C,i}^2 + x_{C,q}^2. \tag{29}$$

The random variables $x_{C,i}$ and $x_{C,q}$ are Gaussian with pdfs

$$x_{C,i} \sim \text{N}\left(\sqrt{(1-\Omega)S},\ \frac{\Omega S + 2\sigma_n^2}{2M}\right) \tag{30}$$

$$x_{C,q} \sim \text{N}\left(0,\ \frac{\Omega S + 2\sigma_n^2}{2M}\right), \tag{31}$$

so P_C in (29) is a noncentral chi-squared random variable with 2 degrees of freedom. We can express P_C in terms of the standard noncentral chi-squared pdf by defining the normalized random variables

$$x'_{C,i} = \frac{x_{C,i}}{\sqrt{(\Omega S + 2\sigma_n^2)/(2M)}} \sim \text{N}\left(\sqrt{\frac{(1-\Omega)S}{(\Omega S + 2\sigma_n^2)/(2M)}},\ 1\right) \tag{32}$$

$$x'_{C,q} = \frac{x_{C,q}}{\sqrt{(\Omega S + 2\sigma_n^2)/(2M)}} \sim \text{N}\left(0,\ 1\right). \tag{33}$$

Then

$$P_C = P'_C \cdot \frac{\Omega S + 2\sigma_n^2}{2M} \tag{34}$$

where

$$P'_C = \left(x'_{C,i}\right)^2 + \left(x'_{C,q}\right)^2 \tag{35}$$

$$\sim \chi^2\left(2, \delta\right) \tag{36}$$

$$\delta = \frac{(1-\Omega)S}{(\Omega S + 2\sigma_n^2)/(2M)} \tag{37}$$

and $\chi^2\left(2, \delta\right)$ denotes a standard noncentral chi-squared pdf with 2 degrees of freedom and noncentrality parameter δ. The pdf for P_C in (29) can be expressed as[1]

$$f_{P_C}(p) = \frac{1}{(\Omega S + 2\sigma_n^2)/M} \exp\left(-\frac{p + (1-\Omega)S}{(\Omega S + 2\sigma_n^2)/M}\right) I_0\left(\frac{2\sqrt{p(1-\Omega)S}}{(\Omega S + 2\sigma_n^2)/M}\right) H(p), \tag{38}$$

where $I_0(\cdot)$ is the modified Bessel function of the first kind with order 0, and $H(p)$ is the unit step function with $H(p) = 0$ for $p < 0$ and $H(p) = 1$ for $p \geq 0$.

---

[1]The random variable $\sqrt{P_C}$ has a Rician distribution, which is commonly used to model fading communication channels with a "direct path." The direct path corresponds to the nonzero mean in (30).

The mean and variance of P_C are developed as follows. In general, if $P' \sim \chi^2(D, \delta)$, i.e., P' is a standard noncentral χ^2 random variable with D degrees of freedom and parameter δ, then [17]

$$P' \sim \chi^2(D, \delta) \tag{39}$$

$$E\{P'\} = D + \delta \tag{40}$$

$$\mathrm{Var}\{P'\} = 2(D + 2\delta). \tag{41}$$

Applying these to P_C using (34)-(37) yields

$$E\{P_C\} = (1 - \Omega)S + \frac{\Omega S + 2\sigma_n^2}{M} \tag{42}$$

$$\mathrm{Var}\{P_C\} = \frac{\Omega S + 2\sigma_n^2}{M}\left[\frac{\Omega S + 2\sigma_n^2}{M} + 2(1 - \Omega)S\right]. \tag{43}$$

Note from (42) that P_C is a biased estimate of S, which is not surprising. For large M, $E\{P_C\} \to (1-\Omega)S$, which corresponds to the average power of the *unscattered* component of the source signal. The variance expression (43) shows the benefit of coherently averaging M samples.

Incoherent combining: Incoherent combining of the M independent complex envelope samples with pdfs in (27) yields the average power of the measured signal as

$$P_I = \frac{1}{M}\sum_{m=1}^{M}|\tilde{x}(t_m)|^2 = \frac{1}{M}\sum_{m=1}^{M}\left[x_i(t_m)^2 + x_q(t_m)^2\right]. \tag{44}$$

Normalizing the random variables analogously to (32)-(34), it follows that P_I is a noncentral chi-squared random variable with $2M$ degrees of freedom:

$$P_I' = \frac{P_I}{(\Omega S + 2\sigma_n^2)/(2M)} \tag{45}$$

$$\sim \chi^2(2M, \delta) \tag{46}$$

$$\delta = \frac{(1 - \Omega)S}{(\Omega S + 2\sigma_n^2)/(2M)}. \tag{47}$$

Note that the noncentrality parameter δ is identical in (37) and (47) for coherent and incoherent combining. The only difference between the coherent and incoherent cases is the number of degrees of freedom in the chi-squared random variable: 2 degrees of freedom in (36) for coherent combining, and $2M$ degrees of freedom in (46) for incoherent combining. The pdf for P_I in (44) can be expressed as

$$f_{P_I}(p) = \frac{1}{(\Omega S + 2\sigma_n^2)/M}\left(\frac{p}{(1 - \Omega)S}\right)^{(M-1)/2}\exp\left(-\frac{p + (1 - \Omega)S}{(\Omega S + 2\sigma_n^2)/M}\right) \cdot$$

$$I_{M-1}\left(\frac{2\sqrt{p(1 - \Omega)S}}{(\Omega S + 2\sigma_n^2)/M}\right)H(p), \tag{48}$$

where $I_{M-1}(\cdot)$ is the modified Bessel function of the first kind with order $M - 1$. The mean and

variance of P_I are

$$E\{P_I\} = S + 2\sigma_n^2 \quad \text{(independent of } M\text{)} \tag{49}$$

$$\text{Var}\{P_I\} = \frac{\Omega S + 2\sigma_n^2}{M} \left[(\Omega S + 2\sigma_n^2) + 2(1 - \Omega)S \right] \tag{50}$$

$$= \frac{1}{M} \left[E\{P_I\}^2 - (1 - \Omega)^2 S^2 \right] \tag{51}$$

$$= \frac{1}{M} \left[\text{SNR}^{-1} \left(2 + \text{SNR}^{-1} \right) + \Omega \left(2 - \Omega \right) \right] S^2 \tag{52}$$

$$\rightarrow \frac{1}{M} \Omega \left(2 - \Omega \right) S^2 \text{ for large SNR,} \tag{53}$$

where $\text{SNR} \triangleq S/(2\sigma_n^2)$. For the large SNR case, one standard deviation above and below the mean of P_I can be expressed as follows, in dB:

$$10 \log_{10} \left(S + \sqrt{\text{Var}\{P_I\}} \right) = 10 \log_{10} S \ + \ 10 \log_{10} \left[1 + \sqrt{\Omega(2 - \Omega)/M} \right] \tag{54}$$

$$10 \log_{10} \left(S - \sqrt{\text{Var}\{P_I\}} \right) = 10 \log_{10} S \ + \ 10 \log_{10} \left[1 - \sqrt{\Omega(2 - \Omega)/M} \right]. \tag{55}$$

Thus in dB, the size of the ± 1 standard deviation "error bars" for P_I are independent of the signal strength, S. An example is presented in Section 3 that evaluates (54) and (55) for a scenario with a harmonic signal.

Comparing the variance expressions in (43) and (50) for coherent and incoherent combining, $\text{Var}\{P_C\} \leq \text{Var}\{P_I\}$, as expected. Next let us compare the mean expressions in (42) and (49) for large M in a scattering medium with $0 < \Omega < 1$. Then

$$|S - E\{P_C\}| \approx \Omega S \tag{56}$$

$$|S - E\{P_I\}| = 2\sigma_n^2. \tag{57}$$

If the $\text{SNR} = S/(2\sigma_n^2)$ is large, then the incoherent P_I may have smaller bias with respect to S than the coherent P_C, but P_C has smaller variance than P_I. The incoherent combining tends to collect *all* of the signal power (unscattered and scattered). The coherent combining collects the unscattered signal power while reducing the scattered signal power and noise by averaging.

For $M = 1$ sample, P_C and P_I are identical. Figure 2(a) shows plots of the pdf of $10 \log_{10}(P)$ for $M = 1$, $S = 1$, and $\text{SNR} \triangleq 1/(2\sigma_n^2) = 10^3 = 30$ dB. Note that a small deviation in the saturation Ω from 0 causes a significant spread in the distribution of received power P around the unscattered signal power, $S = 1$ (0 dB). This variation in P will limit the performance of classification algorithms that use P as a feature.

Model for multiple harmonics: For each harmonic frequency $l f_0$, with $l = 1, \ldots, L$, processing structures as in Figure 1 may be used to obtain the complex envelopes, $\widetilde{x}_1(t), \ldots, \widetilde{x}_L(t)$. For the lth harmonic, the sinusoids in Figure 1 are changed to $\cos(2\pi l f_0 t)$, $\sin(2\pi l f_0 t)$. Each harmonic, l, is characterized by average signal power S_l, saturation Ω_l, and average noise power $2\sigma_n^2$, so that M samples of the complex envelope at each harmonic are modeled as in (27):

$$\widetilde{x}_l(t_m) \sim \text{CN} \left(\sqrt{(1 - \Omega_l)S_l} \, e^{j\theta_{l,m}}, \ \Omega_l S_l + 2\sigma_n^2 \right), \quad l = 1, \ldots, L, \ m = 1, \ldots, M. \tag{58}$$

If the time samples $t_1, \ldots, t_M$ are spaced by $> 1/B$ sec, then it is reasonable to model $\widetilde{x}_l(t_1)$, $\ldots, \widetilde{x}_l(t_M)$ as independent for a fixed l. We will also model the scattered signals at different frequencies, $\widetilde{x}_1(t_m), \ldots, \widetilde{x}_L(t_m)$, as independent. Cross-frequency coherence has been studied theoretically

and experimentally, with [14, 15] presenting experimental studies in the atmosphere. However, models for cross-frequency coherence in the atmosphere are at a very preliminary stage. It may be possible to revise our assumption of independent scattering at different harmonic frequencies as better models become available.

In summary, we model all of the random variables in (58) as independent, and the samples at each harmonic may be combined coherently or incoherently, with distributions

$$\text{Coherent:} \qquad P_l = \left| \frac{1}{M} \sum_{m=1}^{M} \widetilde{x}_l(t_m)\, e^{-j\theta_{l,m}} \right|^2, \qquad\qquad l = 1, \ldots, L \qquad (59)$$

$$\sim \frac{\Omega_l S_l + 2\sigma_n^2}{2M} \cdot \chi^2\left(2, \frac{(1 - \Omega_l)S_l}{(\Omega_l S_l + 2\sigma_n^2)/(2M)}\right) \qquad\qquad (60)$$

$$\text{Incoherent:} \qquad P_l = \frac{1}{M} \sum_{m=1}^{M} |\widetilde{x}_l(t_m)|^2, \qquad\qquad l = 1, \ldots, L \qquad (61)$$

$$\sim \frac{\Omega_l S_l + 2\sigma_n^2}{2M} \cdot \chi^2\left(2M, \frac{(1 - \Omega_l)S_l}{(\Omega_l S_l + 2\sigma_n^2)/(2M)}\right). \qquad\qquad (62)$$

Our assumptions imply that $P_1, \ldots, P_L$ are independent.

2.2 Saturation model

In [13], Wilson presents models for the saturation parameter as a function of meteorological parameters. Using the reasoning in Appendix A, we obtain from [13] the following approximate model for the saturation under "mostly sunny, calm" conditions:

$$\Omega = 1 - \exp\left(-2 \times 10^{-7} \cdot f^2 \cdot r\right) \qquad\qquad (63)$$

where f is the frequency (in Hz) and r is the range from the source to the sensor (in m). We note that the model in (63) accounts only for scattering due to turbulence in the air, and ground reflections are ignored. To our knowledge, convenient models are not currently available that incorporate ground reflections.

Equation (63) is evaluated and plotted in Figures 2(b)–2(d) to show the variation in saturation Ω with frequency and source range under sunny, calm conditions. Figure 2 indicates that harmonic energy estimates fluctuate by $\pm$ several dB for frequencies above 100 Hz and ranges greater than about 40 m.

3 Classification Performance Based on Propagation Models

The models in the previous section describe the distribution of measured power (P_l) as a function of saturation (Ω_l) at the harmonic frequencies lf_0, $l = 1, \ldots, L$, as well as the variation of Ω_l with frequency (lf_0) and range. The models can be used to study classification performance based on the measured harmonic signature, $\mathbf{P} = [P_1, \ldots, P_L]$, when the "ideal" source signature $\mathbf{S} = [S_1, \ldots, S_L]$ is known in the absence of scattering and sensor noise. Several approaches may be used to study classification performance. For example, suppose a set of C signatures, $\mathbf{S}_1, \ldots, \mathbf{S}_C$, are known that characterize C ground vehicles. Then the probability of classification error can be evaluated analytically. Alternatively, we can study the Cramér-Rao lower bound on the variance of unbiased estimation of $\mathbf{S}$ based on the statistical model for $\mathbf{P}$.
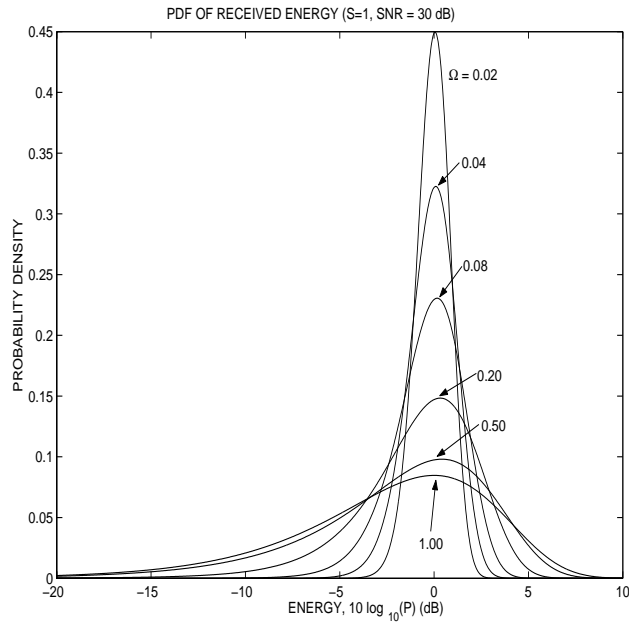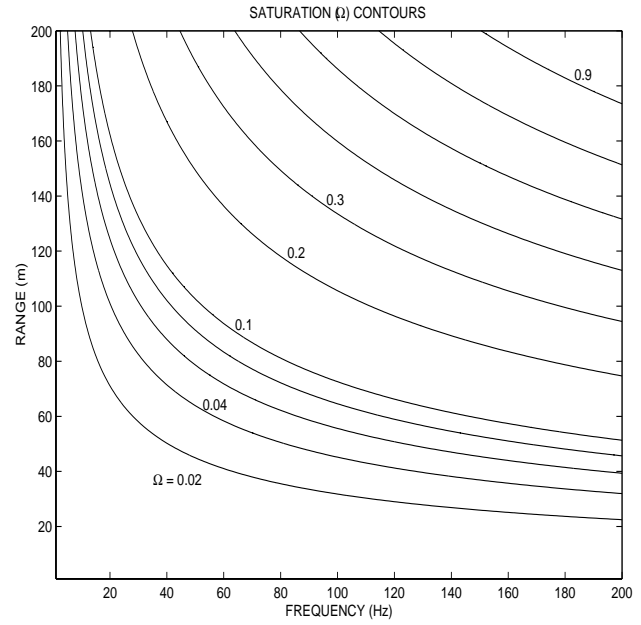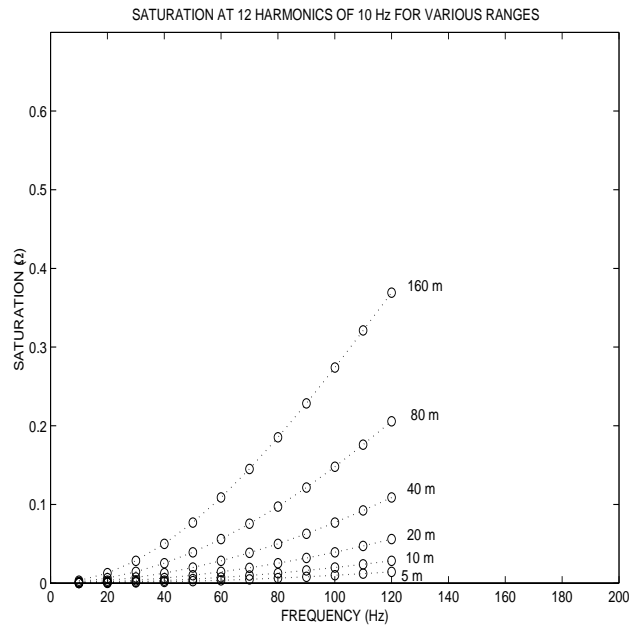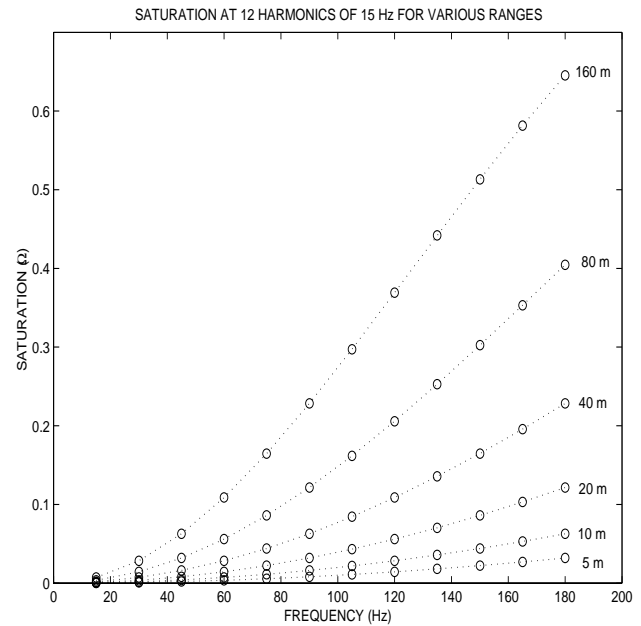
Figure 2: (a) Probability density function (pdf) of average power $10\log_{10}(P)$ measured at the sensor for $M = 1$ sample of a signal with $S = 1$ (0 dB), SNR $= 1/2\sigma_n^2 = 10^3 = 30$ dB, and various values of the saturation, Ω. (b) Variation of saturation Ω with frequency f and range r. The saturation is evaluated at harmonic frequencies corresponding to fundamental frequency $f_0 = 10$ Hz in (c) and $f_0 = 15$ Hz in (d).
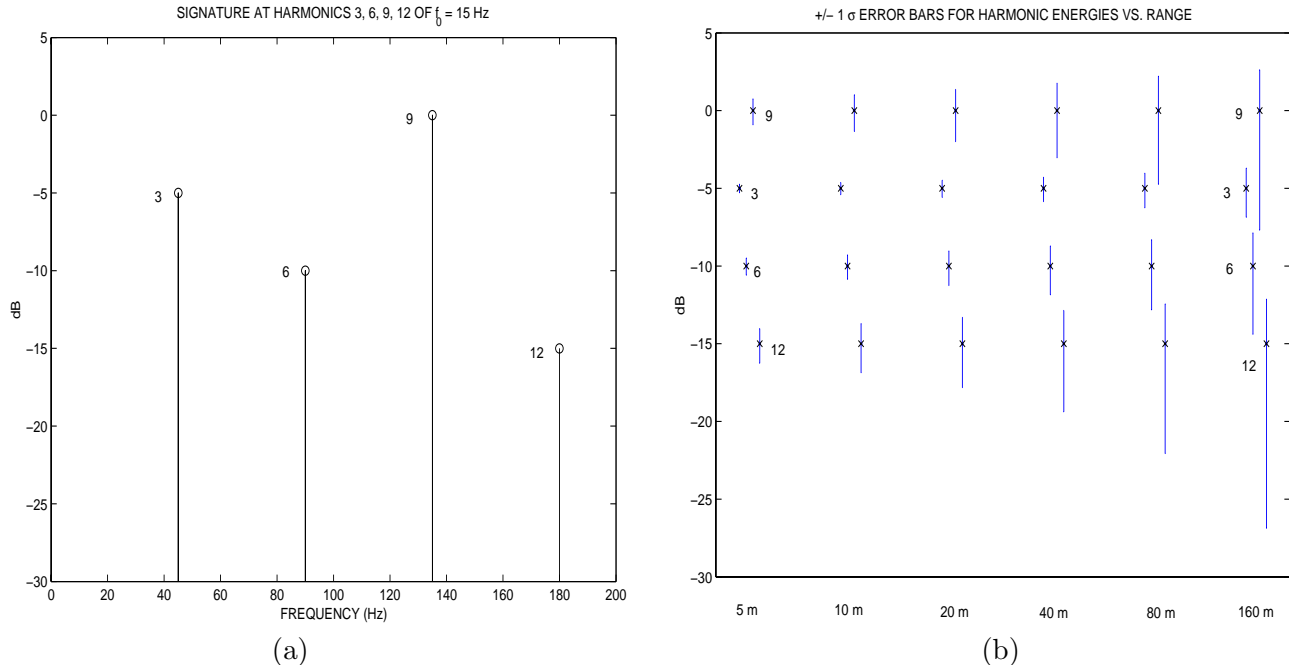
Figure 3: (a) Ideal harmonic signature. (b) Error bars for ± one standard deviation caused by scattering.

We present an example in this section to illustrate the variability in harmonic signatures as the range to the target increases. Consider a harmonic source with fundamental frequency $f_0 = 15$ Hz, and suppose the signature for classification uses harmonics $3, 6, 9$, and 12. We use (54) and (55) to evaluate the ± one standard deviation error bars on the harmonic energy fluctuations under "mostly sunny, calm" meteorological conditions. High SNR is assumed, so the variations are due to scattering during propagation, and we take $M = 1$, i.e., no time averaging. Figure 3(a) shows the "ideal" harmonic signature, and Figure 3(b) shows the error bars for ranges 5, 10, 20, 40, 80, 160 m. At ranges of 80 m and larger, the harmonic components display significant variations, and rank ordering of the harmonic amplitudes would exhibit variations also. Thus classification based on relative harmonic amplitudes would degrade in performance at these ranges.

4   Results from Measured Data

In this section, we examine measured data from ground vehicles in the ACIDS[2] data set provided by the Army Research Laboratory. In particular, we investigate ways to mitigate the harmonic signature fluctuations caused by scattering, and we examine the signature variations with speed and aspect angle. The ACIDS data is recorded at three microphones as a target travels along a straight line, as shown in Figure 4(a). We process the data recorded at microphone 1 in segments of length 1 second. We use a harmonic line association (HLA) algorithm [2] to estimate the fundamental frequency, then we use a Welch power spectral density (PSD) to estimate the energy in narrow bands around the first 12 harmonic frequencies. We normalize the harmonic energy estimates by dividing by the total received energy. This normalization tends to remove the deterministic energy loss caused by spherical spreading of the wavefronts. Note from Figure 4(a) that the time record

---

[2]ACIDS is an acronym for Acoustic-Seismic Classification Identification Data Set.

for each run provides a view of the target at various aspect angles and ranges. The range is large for aspect angles near ±90 degrees, and at these aspect angles the sensor observes the front of the vehicle as it approaches the sensor, and the rear of the vehicle as it departs the sensor. At CPA, the sensor observes the side of the vehicle.

We present plots of the estimated harmonic signatures for "Target 1" and "Target 2" in the ACIDS data set. Both targets are "heavy tracked" vehicles, but they are different types within this class. The estimated energy in the dominant harmonic components for Target 1 at various aspect angles (and ranges) is shown in Figures 4(b) and 4(c). Corresponding results for Target 2 are shown in Figures 4(d) and 4(e). Plots (b) and (d) are at closer CPA range and slower speed, while plots (c) and (e) have larger CPA range and faster speed. We observe from Figures 4(b)–4(e) that the harmonic energy fluctuations are larger at further ranges, which agrees with the scattering propagation models. We also observe that the harmonic signatures are somewhat different when the sensor observes the front of the vehicle, when the sensor observes the rear of the vehicle, and at CPA. For example, harmonic 6 varies with aspect angle for Target 1 in Figure 4(b), and harmonics 3 and 7 vary with aspect angle for Target 2 in Figures 4(d) and 4(e).

These observations suggest that we (incoherently) average the signatures at the front and rear aspects, respectively, to reduce the fluctuations caused by scattering while preserving the aspect-dependent features. Then the averaged front and rear signatures can be used in conjunction with the CPA signature for classification. Figures 5 and 6 contain results for Targets 1 and 2, respectively, that illustrate the aspect-dependent signatures from six runs in the ACIDS data set. There are three runs for each target. Two of the three runs have CPA range of 5 m and speed 15 km/hr, with the vehicle traveling in opposite directions in these two runs. The third run has larger CPA range (25 m) and faster speed (30 km/hr).

Figures 5(a)–5(c) show the harmonic signatures for Target 1 at CPA, front, and rear, respectively. The front and rear results in Figures 5(b) and 5(c) are obtained by averaging 10 signatures, measured at different times at aspect angles near ±90 degrees. The CPA signature in Figure 5(a) contains no averaging. Also shown in Figures 5(a)–5(c) by the ∗ is the mean signature at each aspect over the three runs. The mean signatures from Figures 5(a)–5(c) are also plotted in Figure 5(d) to illustrate the variation in harmonic signature with CPA, front, and rear aspects. Note from Figure 5(d) that harmonics 3, 6, and 7 vary by several dB at front and rear aspect angles.

Figure 6 shows corresponding results for Target 2. The mean signatures for front and rear aspect angles in Figure 6(d) show the largest variation at harmonics 3, 6, and 7. Note in Figure 6(d) that harmonics 3 and 7 switch positions as the second-largest harmonic component in the front and rear aspect signatures.

5 Concluding Remarks

We have applied a propagation model to study the statistical fluctuations in harmonic signatures caused by scattering of acoustic signals in the air. The fluctuations are larger at higher frequencies and larger ranges between the source and sensor. The statistical model includes the effect of coherent or incoherent averaging of independent observations of the harmonic signature, and the model may be used to analyze the performance limits of classifiers based on harmonic line signatures. If meteorological data is available to provide an estimate of the saturation level in the atmosphere, then the model may be used in a real-time system to predict when classification is unreliable due to excessive scattering.

We examined measured data in the Army Research Laboratory's ACIDS data set to assess the variability of ground vehicle harmonic signatures with range, speed, and aspect angle. The harmonic
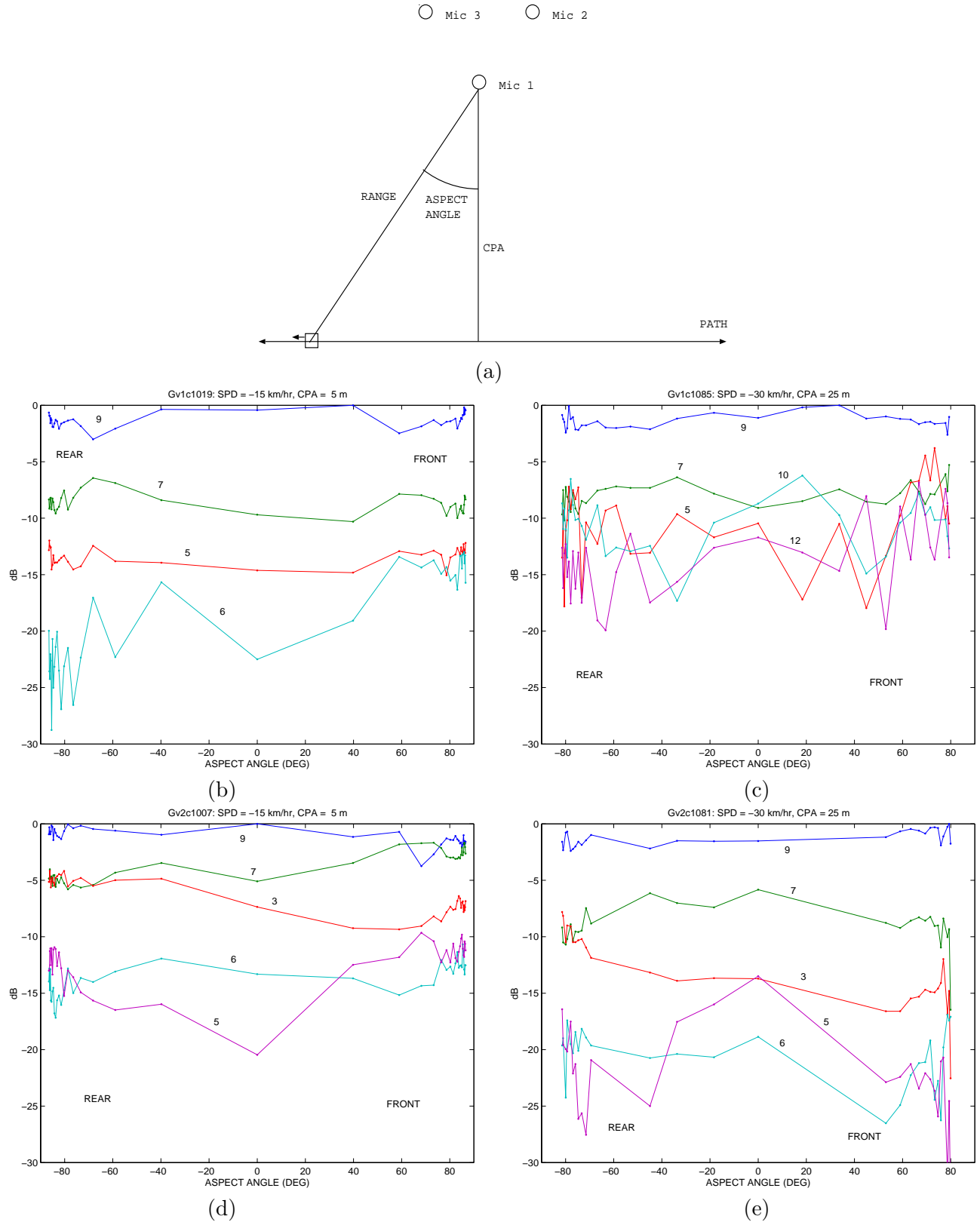
Figure 4: (a) Sensors and target path for ACIDS data. (b) and (c): Energy in dominant harmonics for Target 1. (d) and (e): Energy in dominant harmonics for Target 2. (c) and (e) have larger CPA range and faster speed than (b) and (d).
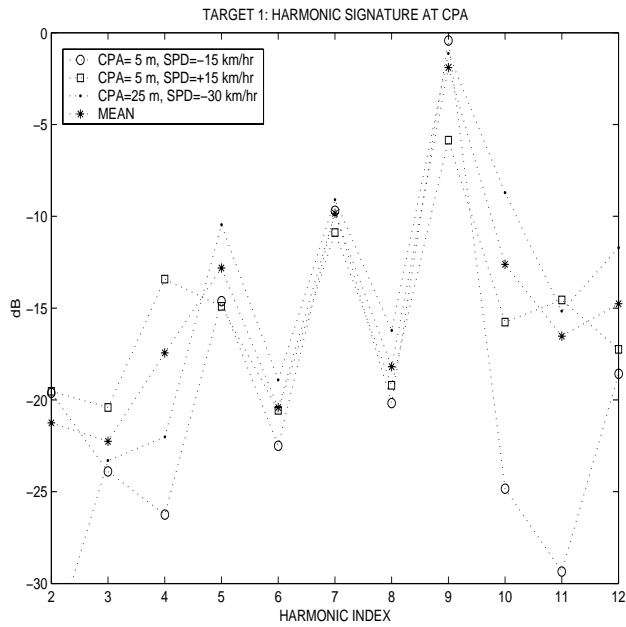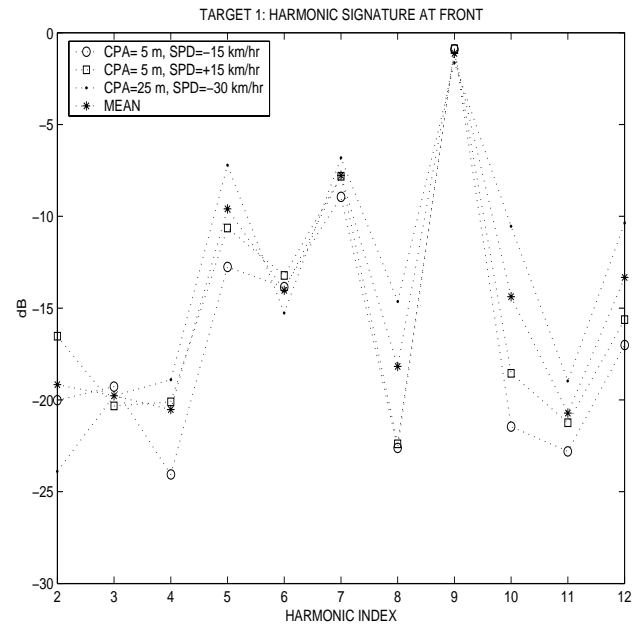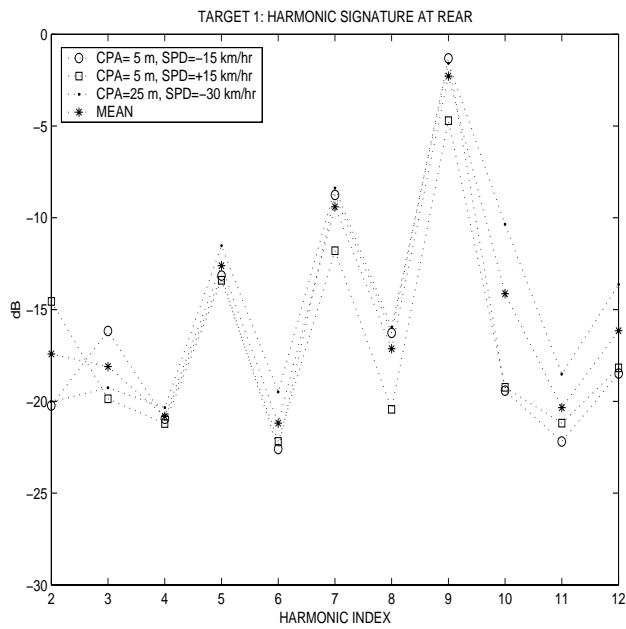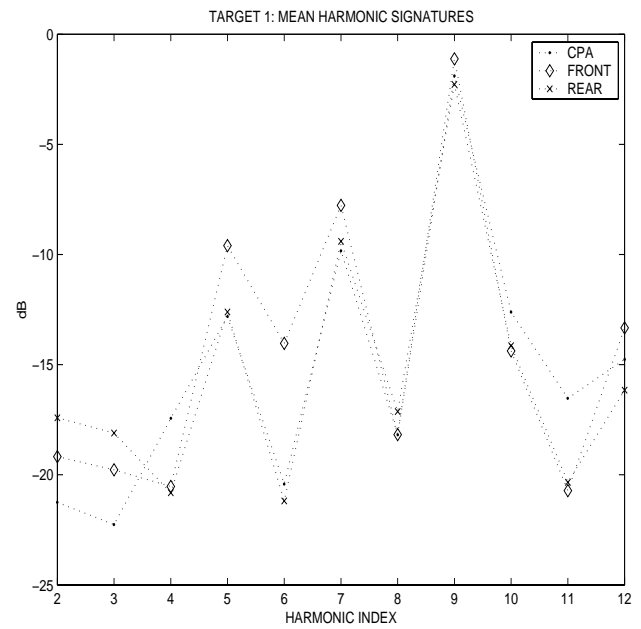
Figure 5: Harmonic signatures for Target 1 for three runs. (a) CPA signature. (b) Average of 10 signatures at front aspect. (c) Average of 10 signatures at rear aspect. (d) Mean signatures over the three runs at CPA, front, and rear aspects.
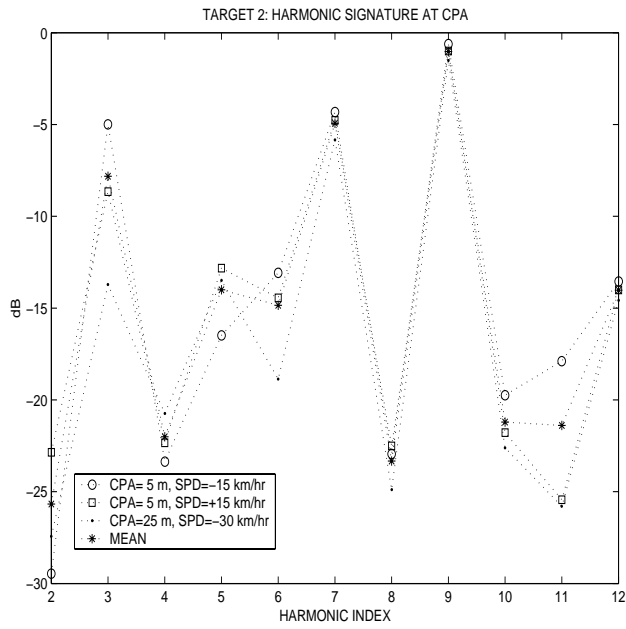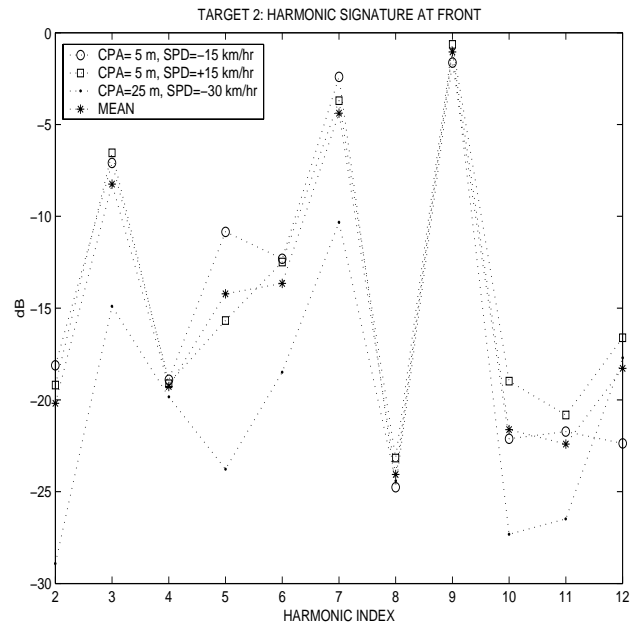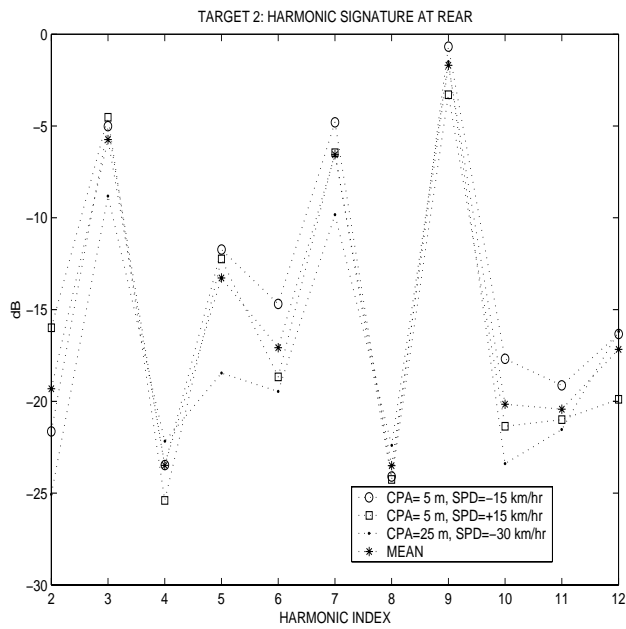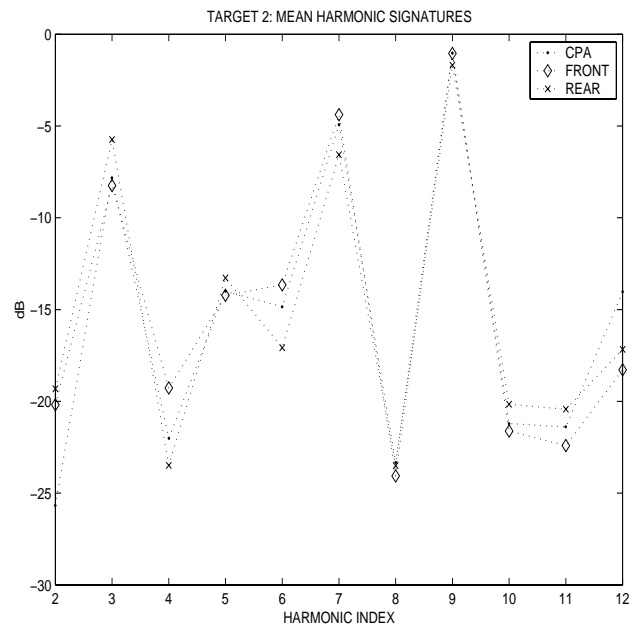
Figure 6: Harmonic signatures for Target 2 for three runs. (a) CPA signature. (b) Average of 10 signatures at front aspect. (c) Average of 10 signatures at rear aspect. (d) Mean signatures over the three runs at CPA, front, and rear aspects.

signatures exhibit larger fluctuations at larger ranges, as predicted by the model. The harmonic signature variations with source aspect angle may be coarsely quantized into three cases: CPA (side of target), front of vehicle, and rear of vehicle. Furthermore, several independent estimates of the harmonic signature are typically available at the front and rear aspects, so these may be averaged to reduce the fluctuations in the signature due to scattering. We showed the harmonic signatures at CPA, front, and rear aspects for Targets 1 and 2 in the ACIDS data set. We observed that the energy level of some harmonics varied by several dB at the front and rear aspects. Although results for only two targets were included in this paper, we observed similar behavior in the harmonic signatures of most targets in the data set.

The results in this paper considered a limited set of target speeds, ranges, and meteorological conditions. We will examine a larger variety of conditions in future work. We are also working with the ACIDS data set to quantify the improvement in classification performance that is enabled when aspect-dependent signatures are used.

Acknowledgment

Appendix

A   Rationale for Scattering Model

This appendix provides an outline of the reasoning behind the model for saturation in (63).

1. Following [12], equations (13) and (16) imply

$$\Omega = 1 - \exp\left(-\alpha(\infty) \cdot r\right), \tag{64}$$

    where r is used for the range in (64) instead of x that is used in [12]. The extinction coefficient $\alpha(\rho)$ for the second moment is described in (15) of [12] as

$$\alpha(\rho) = 2\pi k^2 \left[f(0) - f(\rho)\right] \tag{65}$$

$$\text{where } k = \frac{2\pi f}{c_0} \quad (f = \text{frequency, in Hz}) \tag{66}$$

$$c_0 = \text{speed of sound} \tag{67}$$

$$\rho = \text{sensor separation, transverse to the propagation direction} \tag{68}$$

$$f(\rho) = \text{two-dimensional correlation function for sound-speed fluctuation.} \tag{69}$$

2. We need to find $\alpha(\rho)$ for large ρ, and use this value as $\alpha(\infty)$ in (64). It is shown in [13] that the factor $[f(0) - f(\rho)]$ in (65) initially increases monotonically with ρ, but then it saturates when ρ is between 100 m and 1,000 m (see Figure 4 in [13]). Therefore according to (65) and (66), for large enough ρ,

$$\alpha(\infty) = \xi f^2, \tag{70}$$

    where ξ is a constant that depends on the atmospheric conditions.

3. We obtained a rough estimate for the value of ξ using the top-left panel in Figure 5 in [13] for "mostly sunny, calm" conditions. Assuming that the largest value of ρ in the figure, 100 m, is "large enough" for $\alpha(\infty)$, the following values are estimated from the plot:

f (Hz)	20	70	200	700
$\alpha(100)^{-1}$	10^4	10^3	10^2	10

Using these values in (70) yields a value for $\xi \approx 2 \times 10^{-7}$. Then using $\xi = 2 \times 10^{-7}$ in (70), and inserting (70) in (64) yields the model for Ω in (63).

We note that it may be possible using results in [16] to directly model the saturation in terms of the "squared strength parameter" $\Phi^2 \stackrel{\triangle}{=} \alpha(\infty)r$.

References

[1] N. Srour and J. Robertson, "Remote netted acoustic detection system," Army Research Laboratory, ARL-TR-1166, May 1995.

[2] M. Wellman, N. Srour, and D.B. Hillis, "Acoustic feature extraction for a neural network classifier," Army Research Laboratory, ARL-TR-1166, Jan. 1997.

[3] N. Srour, D. Lake, and M. Miller, "Utilizing acoustic propagation models for robust battlefield target identification," *Proc. 1998 Meeting of the IRIS Specialty Group on Acoustic and Seismic Sensing*, Sept. 1998.

[4] D. Lake, "Robust battlefield acoustic target identification," *Proc. 1998 Meeting of the IRIS Specialty Group on Acoustic and Seismic Sensing*, Sept. 1998.

[5] D. Lake, "Efficient maximum likelihood estimation for multiple and coupled harmonics," Army Research Laboratory, ARL-TR-2014, Dec. 1999.

[6] D. Lake, "Harmonic phase coupling for battlefield acoustic target identification," *Proc. IEEE ICASSP*, pp. 2049–2052, 1998.

[7] H. Hurd and T.Pham, "Target association using harmonic frequency tracks," *Proc. Fifth IEEE Int. Conf. on Information Fusion*, pp. 860–864, 2002.

[8] H. Wu and J.M. Mendel, "Data analysis and feature extraction for ground vehicle identification using acoustic data," *2001 MSS Specialty Group Meeting on Battlefield Acoustics and Seismic Sensing*, Johns Hopkins University, Laurel, MD, Oct. 2001.

[9] H. Wu and J.M. Mendel, "Classification of ground vehicles from acoustic data using fuzzy logic rule-based classifiers: early results," *Proc. SPIE AeroSense*, pp. 62–72, Orland, FL, April 1–5, 2002.

[10] D.K. Wilson, B.M. Sadler, T. Pham, "Simulation of detection and beamforming with acoustical ground sensors," *Proc. SPIE 2002 AeroSense Symp.*, Orlando, FL, April 1-5, 2002.

[11] D.K. Wilson, J.T. Kalb, M. Srour, T. Pham, B.M. Sadler, "Sensor algorithm interface and performance simulations in an acoustical battlefield decision aid," ARL Technical Report, 2002.

[12] S.L. Collier and D.K. Wilson, "Performance bounds on atmospheric acoustic sensor arrays operating in a turbulent medium. I. Plane-wave analysis," Technical Report ARL-TR-2426, U.S. Army Research Laboratory, 2800 Powder Mill Road, Adelphi, MD, 20783, 2002.

[13] D.K. Wilson, "Atmospheric effects on acoustic arrays: a broad perspective from models," *1999 Meeting of the IRIA Specialty Group on Battlefield Acoustics and Seismics*, Laurel, MD, September 13-15, 1999.

[14] D.I. Havelock, M.R. Stinson, G.A. Daigle, "Measurements of the two-frequency mutual coherence function for sound propagation through a turbulent atmosphere," *J. Acoust. Soc. Am.*, **104** (1), pp. 91–99, July 1998.

[15] D.E. Norris, D.K. Wilson, and D.W. Thomson, "Correlations between acoustic travel-time fluctuations and turbulence in the atmosphere surface layer", *Acustica*, vol. 87, pp. 677-684, 2001.

[16] D.K. Wilson, "A turbulence spectral model for sound propagation in the atmosphere that incorporates shear and buoyance forcings", *J. Acoust. Soc. Am.*, **108** (5), Pt. 1, pp. 2021–2038, Nov. 2000.

[17] J.M. Bernardo and A.F.M. Smith, *Bayesian Theory*, John Wiley & Sons, West Sussex, England, 1994.